Optical and Quantum Electronics **34:** 661–675, 2002.

Two-dimensional field analysis of semiconductor lasers with small vertical beam divergence

GRAY LIN AND CHIEN PING LEE*
*Department of Electronics Engineering, National Chiao Tung University, Hsinchu, Taiwan, Republic of China (*author for correspondence: E-mail: cplee@cc.nctu.edu.tw)*

Received 12 December 2000; accepted 28 December 2000

Abstract. Two-dimensional (2D) optical field distribution and the far-field patterns are analyzed for semiconductor lasers with small vertical beam divergence. The discrete spectral index method is used for the analysis and compared with other methods such as the effective index method. The discrete spectral index method is found to be much better in terms of accuracy and computation efficiency for the laser structures studied. Two laser structures with experimental counterparts are studied. The best beam aspect ratio (<1.5) is achieved using the conventional ridge waveguide process. The calculated results compare very favorably with the experimental results. Simulations also reveal the guidelines for design of symmetric optical beam.

Key words: beam aspect ratio, beam divergence, discrete spectral index method, ridge waveguide laser, two-dimensional analysis

1. Introduction

Semiconductor lasers with small vertical beam divergence have drawn much interest in recent years (Temmyo and Sugo 1995; Ziari *et al.* 1995; Lin *et al.* 1996). The key to the design of such lasers is to have a wide near field distribution in the cladding without much affecting the field confinement in the quantum well (QW) active region (Yen and Lee 1996). With lower index antiguiding layers inserted between the cladding layers and the graded-index (GRIN) layers, we can reduce the vertical beam divergence down to 15° and below with reasonable threshold current (Lin *et al.* 1996). The advantages of this type of lasers are higher coupling efficiency to fibers and relaxed package alignment tolerance (Ziari *et al.* 1995).

Previous designs on lasers with small vertical beam divergence are usually based on one-dimensional (1D) simulations along the layer growth direction. But because of the mode profiles and the far field patterns are nearly symmetrical, 1D simulation is not enough to adequately describe the mode characteristics.

In this paper, we investigate the 2D optical field distribution in narrow beam stripe geometry lasers. Only fundamental TE mode is considered throughout this simulation. Discrete spectral index (DSI) method (Berry *et al.* 1995) rather than conventional effective index method (EIM) or purely numerical finite difference method (FDM) was used in the 2D simulation. In the following section, we first discuss why EIM does not apply for lasers with small vertical beam divergence and then the basics for DSI are reviewed. The analytical expression for the far-field distribution is also derived in this section. The boundary condition of finite cladding thickness is adopted in the simulation. Then, the experimental and simulation results are given and compared in Section 3. Simulation is also conducted for design of symmetric beam profile. Finally, we draw a conclusion in Section 4.

2. Theoretical background

2.1. SIMULATION METHOD

For lasers with ridge waveguide structures, a quasi 2D simulation based on EIM is usually used, for which the field solutions are assumed to be separable in the transverse and lateral directions. Because of the discontinuities introduced at the rib edges, the electric field profile is discontinuous and this leads to a structure dependent accuracy problem. The EIM becomes inaccurate if the rib height is large compared with the guiding layer thickness, or if the rib height is comparable to the rib width. This is because the approximation used in this method, namely that the waveguide can be considered as three distinct regions, breaks down when the field values on each side of the rib are very different. Although the EIM method, based on 1D analysis, gives approximately the correct size for the guided modes, it fails completely to describe the shape of the mode.

The purely numerical techniques, such as finite difference (FD) and finite element (FE) methods, can correctly model general waveguide structures. But they are computation-intensive and are not necessarily the practical tools for solving a particular problem. For the investigated laser structure, GRIN QW laser with small vertical beam divergence, since the layer structure is complicated and the mode index is very close to the refractive index of the waveguide cladding, the mesh size has to be sufficiently small for accurate calculation. The requirement of large computational resources will render these purely numerical techniques impractical.

The semi-analytic DSI method, developed for semiconductor rib structure, has the advantages of extremely short computing-time and high accuracy. We found that the DSI method is extremely useful in the 2D analysis of lasers with small beam divergence.

2.2. THE DISCRETE SPECTRAL INDEX METHOD

The spectral index method is based on a simple axiom that if one knows the eigenvalue equation for the propagation constant, β, one can reconstruct the field profile, $E(x, y)$. The spectral index method proceeds by (i) finding a simple solution to the wave equation inside the rib, (ii) finding a Fourier series or Fourier transform of the solution in the layered region below the rib, and (iii) using a variational boundary condition to join the two together (Robson and Kendall 1990). It is the latter boundary condition which constraints the value of β, and so leads to the eigenvalue equation.

The 2D scalar wave equation is expressed as

$$\frac{\partial^2 E}{\partial x^2} + \frac{\partial^2 E}{\partial y^2} + (k_j^2(x, y) - \beta^2)E = 0, \tag{1}$$

where $E(x, y, z) = E(x, y)\exp(-\mathrm{j}\beta z)$, with $E(x, y)$ the electric field profile, n_j the refractive index of the jth layer, λ the free-space wavelength, β the propagation constant, $k_0 = 2\pi/\lambda$ and $k_j = 2\pi n_j/\lambda$.

In order to find the solution of simple analytic form to the wave equation inside the rib, we should first redefine the air–semiconductor interface (refer to Fig. 1) according to the method of effective widths (MoEW) (Adams 1981). The MoEW compensates for the slight penetration of the field into air such that the field is set to zero along the repositioned air–semiconductor interface, i.e.,

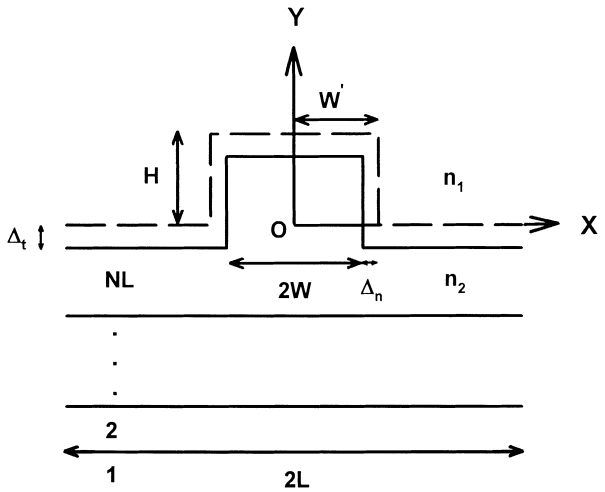

Fig. 1. The coordinate system used for discrete spectral index method. The y origin is in the plane of the base of the effective rib, rather than the physical rib.

$$E_{\mathrm{I}}(\pm W', y) = 0; \;\; E_{\mathrm{I}}(x, +H) = 0. \tag{2}$$

The additional thickness or the decay lengths Δ_n and Δ_t for TE mode are defined as

$$\Delta_n = \frac{n_1^2}{n_2^2} \frac{1}{k_0 \sqrt{n_{\mathrm{e}}^2 - n_1^2}}; \quad \Delta_t = \frac{1}{k_0 \sqrt{n_{\mathrm{e}}^2 - n_1^2}} \tag{3}$$

with $n_{\mathrm{e}} \equiv \beta / k_0$. The solution for symmetric modes, matching the above boundary conditions, can therefore be written in the form

$$E_{\mathrm{I}}(x, y) = \sum_{m=1}^{\infty} \cos(S_m x) \; G_m(y); \quad S_m = (2m - 1) \frac{\pi}{2W'} \tag{4}$$

for $|x| \leq W'$; $0 \leq y \leq H$, where

$$G_m(y) = -A_m \frac{\sin(\gamma_m (y - H))}{\sin(\gamma_m H)}; \quad \gamma_m^2 = (k^2 - S_m^2 - \beta^2) \tag{5}$$

and β is the propagation constant.

For the layered region below the rib ($y < 0$), the solution for symmetric modes, vanishing at $x = \pm L$, can be written in the form of the Fourier series

$$E_{\mathrm{II}}(x, y) = \sum_{q=1}^{\infty} \cos(S_q x) \, G_q(y); \quad S_q = (2q - 1) \frac{\pi}{2L} \tag{6}$$

for $|x| \leq L$; $y \leq 0$. Substituting Equation (6) into the wave equation, we obtain the 1D Fourier-transformed wave equation for a particular spectral component q in the jth layer below the rib, i.e.,

$$\frac{\partial^2 G_q}{\partial y^2} - \gamma_j^2(q) G_q = 0 \quad \text{with} \quad \gamma_j^2(q) = -(k_j^2 - S_q^2 - \beta^2). \tag{7}$$

Then the solution of the slab-like Fourier-transformed wave equation obeys the following relationship:

$$\begin{bmatrix} G_q(d_j) \\ G_q'(d_j) \end{bmatrix} = \begin{bmatrix} \cosh(\gamma_j d_j) & \frac{1}{\gamma_j} \sinh(\gamma_j d_j) \\ \gamma_j \sinh(\gamma_j d_j) & \cosh(\gamma_j d_j) \end{bmatrix} \begin{bmatrix} G_q(0_j) \\ G_q'(0_j) \end{bmatrix} \equiv M_j \begin{bmatrix} G_q(0_j) \\ G_q'(0_j) \end{bmatrix}. \tag{8}$$

Here, 0_j and d_j stand for the start and the end position (local coordinate) of the jth layer respectively. The multiple layers below the rib are concatenated

by the boundary conditions for quasi-TE modes and are expressed through the transfer matrix, i.e.,

$$\begin{bmatrix} G_q(d_{\mathrm{NL}}) \\ G'_q(d_{\mathrm{NL}}) \end{bmatrix} = M_{\mathrm{NL}} \cdots M_j \cdots M_2 \begin{bmatrix} G_q(0_2) \\ G'_q(0_2) \end{bmatrix} \equiv M \begin{bmatrix} G_q(0_2) \\ G'_q(0_2) \end{bmatrix}. \tag{9}$$

The solution below the rib ($y < 0$) is linked to the solution in the rib ($y > 0$) by the continuity of electric field, and also by the continuity of stored power at the rib base ($y = 0$). The field continuity gives

$$G_q(0) = \frac{1}{L} \sum_{m=1}^{\infty} G_m(0) \frac{(-1)^{m-1} 2 S_m \cos(S_q W')}{S_m^2 - S_q^2} \tag{10}$$

and the power continuity gives

$$L \sum_{q=1}^{\infty} G_q^2(0)\, \Gamma_{\mathrm{II}}(q) = W' \sum_{m=1}^{\infty} G_m^2(0)\, \Gamma_{\mathrm{I}}(m), \tag{11}$$

where $\Gamma_{\mathrm{I}}(m)$ and $\Gamma_{\mathrm{II}}(q)$ are the transfer functions at the rib base ($y = 0$) for the region in the rib and below the rib, respectively. The transfer function $\Gamma_{\mathrm{I}}(m)$ in the rib is defined by,

$$\Gamma_{\mathrm{I}}(m) \equiv \frac{G'_m(0)}{G_m(0)} = -\gamma_m \cot(\gamma_m H), \tag{12}$$

while the transfer function $\Gamma_{\mathrm{II}}(q)$ below the rib is defined by,

$$\Gamma_{\mathrm{II}}(q) \equiv \frac{G'_q(0)}{G_q(0)} = \frac{G'_q(d_{\mathrm{NL}})}{G_q(d_{\mathrm{NL}})} = \frac{M_{21} + M_{22}\Gamma_2(q)}{M_{11} + M_{12}\Gamma_2(q)}, \tag{13}$$

where

$$\Gamma_2(q) \equiv \frac{G'_q(0_2)}{G_q(0_2)} = \frac{G'_q(d_1)}{G_q(d_1)} = \gamma_1(q). \tag{14}$$

Here, $y = 0$ stands for the plane of rib base (global coordinate), and M is the transfer matrix defined in Equation (9). Equation (14) comes from the boundary condition that only the outward-going wave exists in the first layer. Combining Equations (10) and (11) with the transfer functions introduced above gives the transcendental equation for β in a closed form, which is

$$\Gamma_{\mathrm{I}}(m)G_m(0) = \frac{1}{W'L}\sum_{n=1}^{\infty} G_n(0)\sum_{q=1}^{\infty}\frac{(-1)^{m-1}2S_m\cos(S_qW')}{S_m^2 - S_q^2} \times \frac{(-1)^{n-1}2S_n\cos(S_qW')}{S_n^2 - S_q^2}\Gamma_{\mathrm{II}}(q). \tag{15}$$

2.3. FAR-FIELD PROFILE

If we neglect the longitudinal field component of the mode, the radiation field amplitude at large distance is given by (Clarke 1983),

$$e(S_x, S_y) = \Psi(\theta_x, \theta_y)\iint_{\Omega} \mathrm{d}x\,\mathrm{d}y\,E(x,y)\,\exp\left[\mathrm{j}(S_x x + S_y y)\right], \tag{16}$$

where $S_x = k_0\sin\theta\cos\phi \equiv k_0\sin\theta_x$, $S_y = k_0\sin\theta\sin\phi \equiv k_0\sin\theta_y$ and $\Psi(\theta_x, \theta_y)$ is the obliquity factor, and where θ is the polar angle to the z axis, ϕ is the corresponding azimuthal angle, and θ_x and θ_y are the component θ resolved along x and y. Here, the obliquity factor is assumed to be equal to $\cos(\theta)$ for both TE and TM modes in all our numerical calculations (Clarke 1983).

The 2D integral of FFP can be reduced to two 1D integrals due to its inherent nature of spectral analysis (Fourier transform), and therefore can be readily evaluated analytically for the multilayer structures. Using the fields defined in Equations (4) and (6), an analytical form for the radiated field amplitude for DSI method can be derived.

2.4. NUMERICAL IMPLEMENTATION

The eigenvalue equation (15) is analytic in mathematical derivation but by no means practical in numerical implementation. In practice, only finite terms of summation are used for the expansion of the field. Let N_m be the number of terms expanding the field in the rib, and N_q be the number of terms for the Fourier series expanding the field below the rib. The boundary length $2L$ is set to be N_w times larger than the rib width $2W$. In choosing a suitable value for L, the bound modes calculated should remain unchanged to any desired accuracy. The set of parameters for numerical implementation is therefore defined by (N_m, N_q, N_w).

Equation (15) is actually a set of N_m linear equations with variables $G_m(0)$. To determine the propagation constant, we require the determinant of this $N_m \times N_m$ matrix to be zero. The Muller's method (Barrodale and Wilson

1978) is used to locate the zeros of the function. Take a look of W' in Equation (15), since W' is itself function of β, as could be seen from Equations (2) and (3), it is equivalent to find the roots of the transcendental equation and therefore is free from the problem of consistency.

2.5. FINITE CLADDING LAYERS

For conventional tightly confined, large vertical beam divergence or low threshold lasers, the thickness of the cladding layer is usually chosen so that the optical field decay to a negligible amount. For such lasers, the thickness of the cladding layer can be treated as infinite and the mode can be analyzed by a simple 1D method. For small vertical beam divergence lasers, since the transverse mode is widely spread into the cladding layer, the infinitely thick cladding approximation can not be used. Besides, for lasers with narrow stripe width, interaction between the transverse and lateral modes would render the consideration of finite cladding thickness very important. Since the optical field decay to zero at finite, instead of infinite, cladding thickness, we

Table 1. The layer structures and the refractive indices of lasers A and B

	Laser A			Laser B		
	Thickness (nm)	AlGaAs (x)	Index (n)	Thickness (nm)	AlGaAs (x)	Index (n)
p-Cladding	3000	0.48	3.22847	3000	0.48	3.22847
p-Antiguiding	100	0.8	3.05539	30	1.0	2.95412
				40	0.48	3.22847
				30	1.0	2.95412
Upper GRIN	100	0.8→0	3.05539→ 3.52340	100	0.8→0	3.05539→ 3.52340
GaAs	12	0	3.52340	12	0	3.52340
InGaAs QW	6	0.25	3.60	5.5	0.226	3.60
GaAs	12	0	3.52340	12	0	3.52340
Lower GRIN	100	0→0.8	3.52340→ 3.05539	100	0→0.8	3.52340→ 3.05539
n-Antiguiding	100	0.8	3.05539	30	1.0	2.95412
				40	0.48	3.22847
				30	1.0	2.95412
n-Cladding	3000	0.48	3.22847	3000	0.48	3.22847

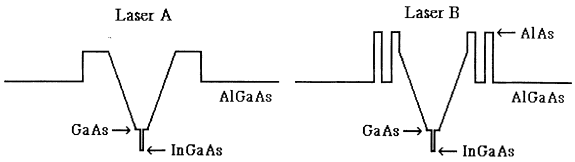

modeled it by putting two fictitious dielectric layers on both sides of the waveguide in the simulation.

3. Results

The DSI method is applied to our newly designed small vertical beam divergence lasers. The layer parameters of the two structures investigated, refer to Laser A and Laser B, are listed in Table 1. Laser A has a 100 nm $Al_{0.8}Ga_{0.2}As$ antiguiding layer on each side of the active region. The optical mode can easily extend beyond these layers into the AlGaAs cladding layers with a lower Al content. But because of these narrow but higher Al content antiguiding layers, the confinement factor for the lasing mode can remain to be high even when the mode is widely spread. In this way small far-field beam divergence can be achieved without sacrificing the threshold current (Yen and Lee 1996). Laser B is similar to Laser A except that the antiguiding layers are replaced by two thin AlAs layers. The thickness of the AlAs layers and the spacing between them are carefully chosen so that the effect of these layers on the mode property is similar to the $Al_{0.8}Ga_{0.2}As$ antiguiding layers in Laser

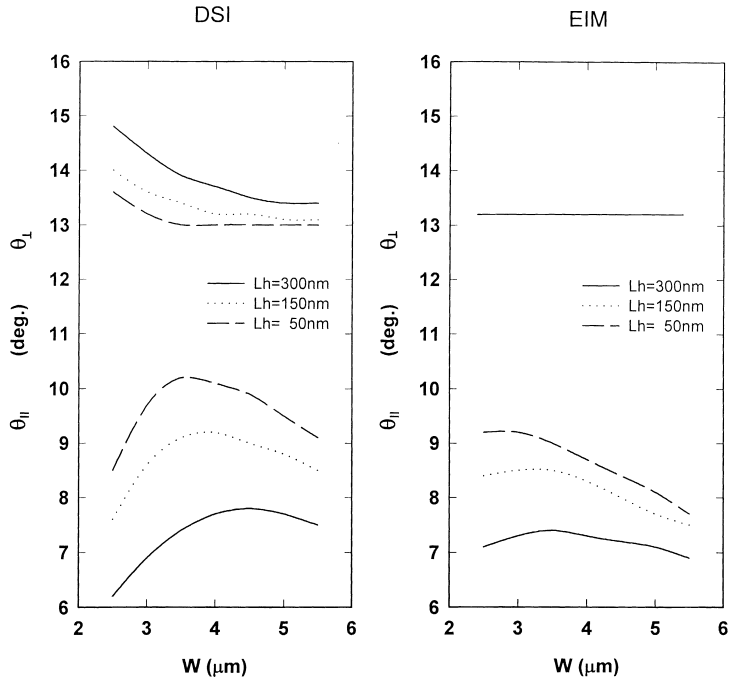

Fig. 2. The calculated (DSI and EIM) vertical far-field angle and lateral far-field angle versus stripe width with dispersion of cladding remaining (L_h) for Laser A.

A. The design wavelength is 980 nm. Finite cladding thickness of 3 μm is used in the simulation and is modeled by putting two fictitious dielectric layers beside the cladding layers. The indices of refraction for $Al_xGa_{1-x}As$ are listed in Table 1 (Afromowitz 1974). The set of parameters for numerical simulation is $(N_m, N_q, N_w) = (5, 64, 8)$.

The calculated results are shown in Figs. 2 and 3, where the vertical far-field angle $\theta_\perp$, and the lateral far-field angle $\theta_\parallel$, are plotted against the stripe width. Both DSI and EIM results are shown for comparison. These sets of curves in the figures correspond to different etching depth for the ridge waveguide. L_h is the thickness of the remaining cladding (measured from the etched surface to the top of the antiguiding layer) outside the ridge. Both laser structures are capable of providing $\theta_\perp$ smaller than 15°. From the DSI results, we can see that the far-field angle depends on both the stripe width and L_h. $\theta_\perp$ decreases slightly with the stripe width and also becomes smaller when the etched depth is deeper (smaller L_h). However, $\theta_\parallel$, first increases and then decreases with the stripe width. It is larger as L_h becomes smaller. For best aspect ratio $\theta_\perp/\theta_\parallel$, the stripe width should be kept around 3.5–5 μm. When $L_h = 50$ nm, the aspect ratio can be as smaller as 1.27. Although very small L_h (or large etched depth) can result in a very small $\theta_\perp/\theta_\parallel$ aspect ratio, the proximity of the etched surface to the laser active region will probably

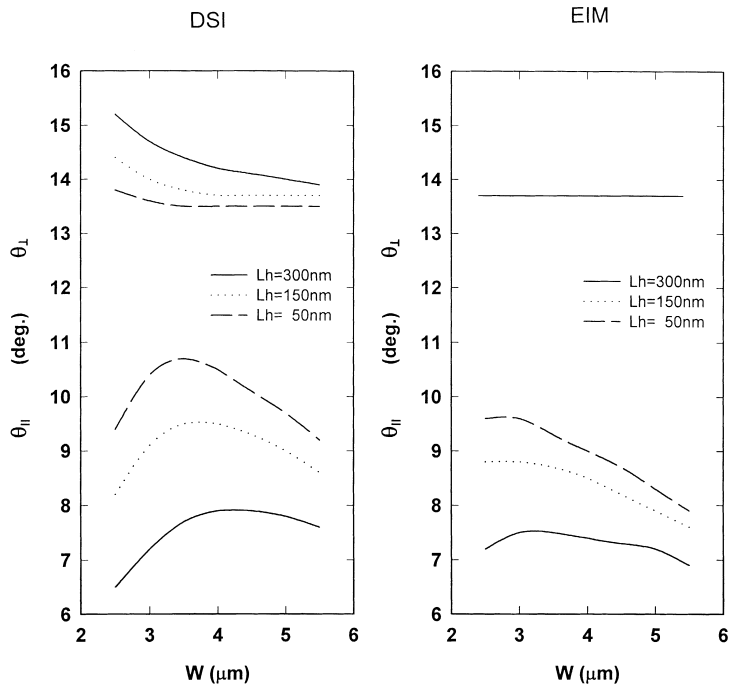

Fig. 3. The same given in Fig. 2 for Laser B.

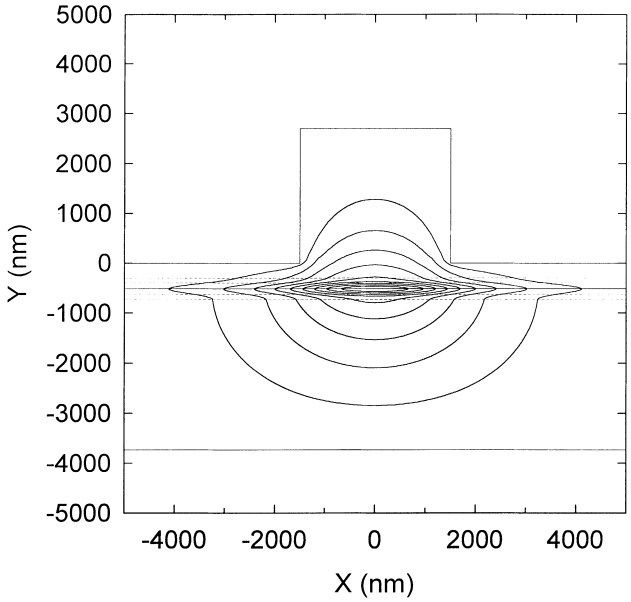

Fig. 4. The near-field contour of Laser A. Contour levels are at the 10% intervels of the maximum field amplitude. The central solid line defines the InGaAs QW, while the dashed lines besides define the antiguiding layers.

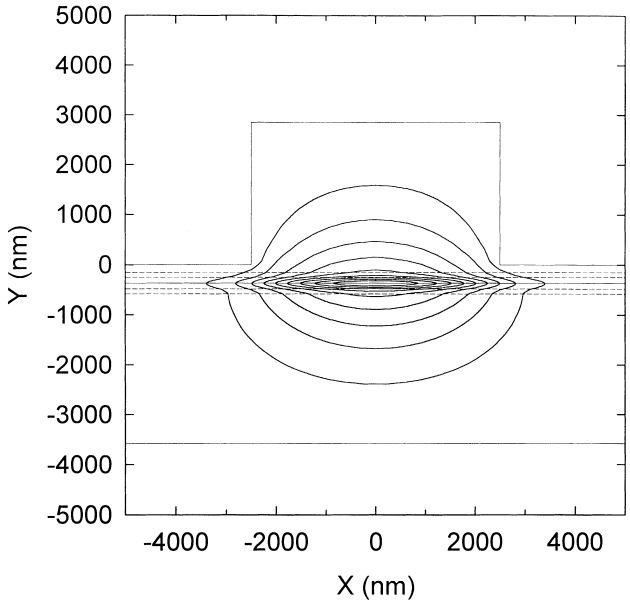

Fig. 5. The near-field contour of Laser B. The conditions and indicators are as given in Fig. 4.

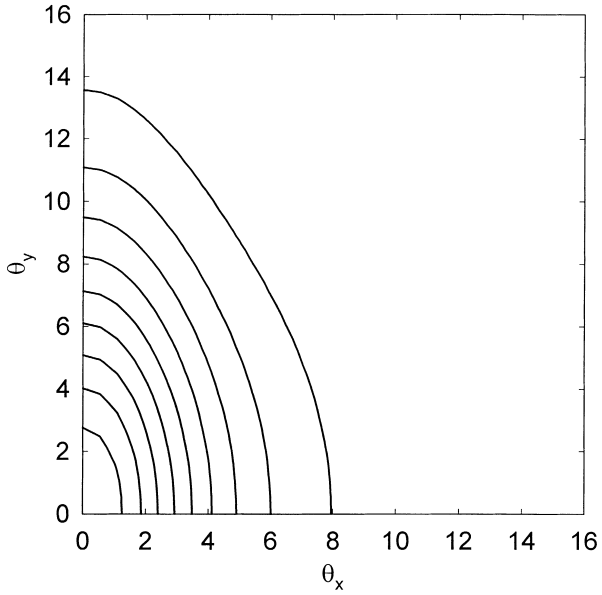

Fig. 6. The far-field contour of Laser A at 10% intervals of maximum field intensity.

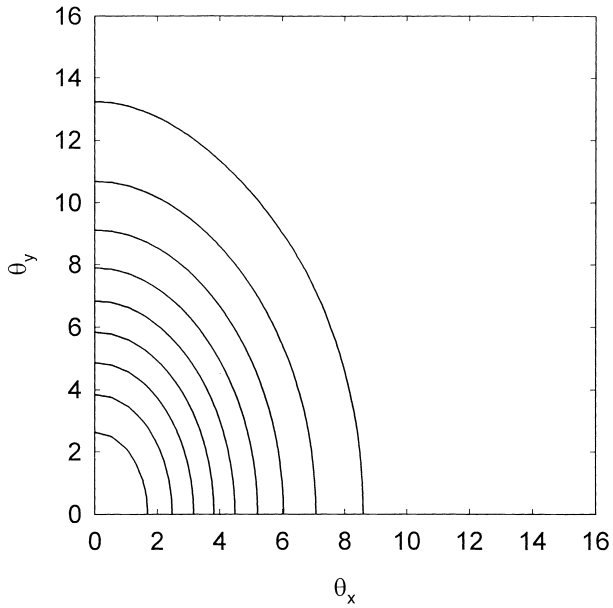

Fig. 7. The far-field contour of Laser B at 10% intervals of maximum field intensity.

degrade the laser performance. So in the following discussion, we will limit L_h in a comfortable range above 150 nm. Take a look at the EIM results, $\theta_\perp$ is

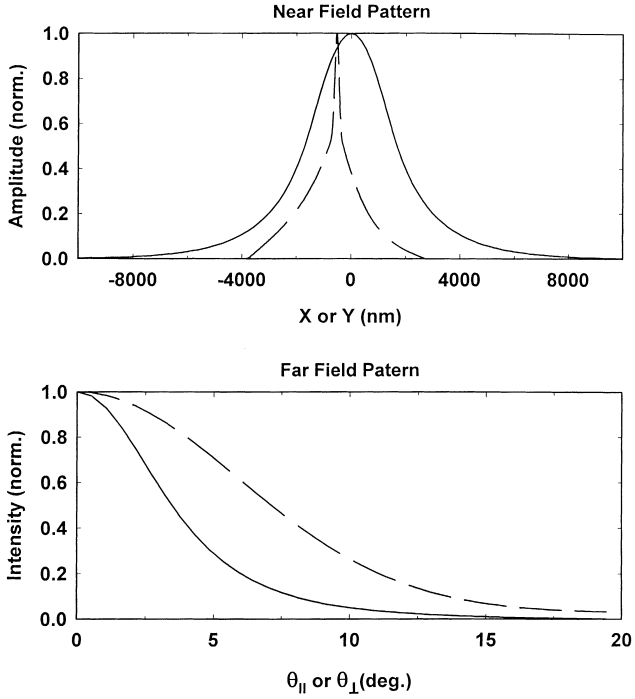

Fig. 8. Cross-section near-field and far-field pattern of Laser A. The solid line is for lateral direction, and the dashed line is for vertical direction.

independent of W while $\theta_{\|}$ shows little dependency at smaller stripe width. The inherent 1D nature of EIM causes an underestimate of beam aspect ratio, and the situation is severe especially for narrow stripe width with large cladding remaining.

For subsequent figures and discussion, we choose $(W, L_h) = (3.0\,\mu\text{m}, 3000\,\text{Å})$ for Laser A, and $(W, L_h) = (5.0\,\mu\text{m}, 1500\,\text{Å})$ for Laser B. Figs. 4 and 5 show the near-field contour plot for Lasers A and B, while the far-field contour plot for Lasers A and B are shown in Figs. 6 and 7, respectively. The cross-sectional near-field distribution at peak amplitude and the far-field intensity radiation pattern along the major axes are shown in Figs. 8 and 9. For Laser A, the far-field angle, defined at half-maximum intensity, is 6.9° laterally and 14.3° vertically, with an aspect ratio of 2.07. While for Laser B, the far-field angle is 9.0° laterally and 13.7° vertically, with an aspect ratio of 1.52. Although the near-field distribution is quite different for vertical and lateral modes, the widely spread transverse mode does reduce the vertical far-field distribution.

The experimental counterparts for Lasers A and B are LM2139 and LM2925, respectively. They have the same layer structure as shown in Table 1. For LM2139, the stripe width is around 3 μm, and the external remaining

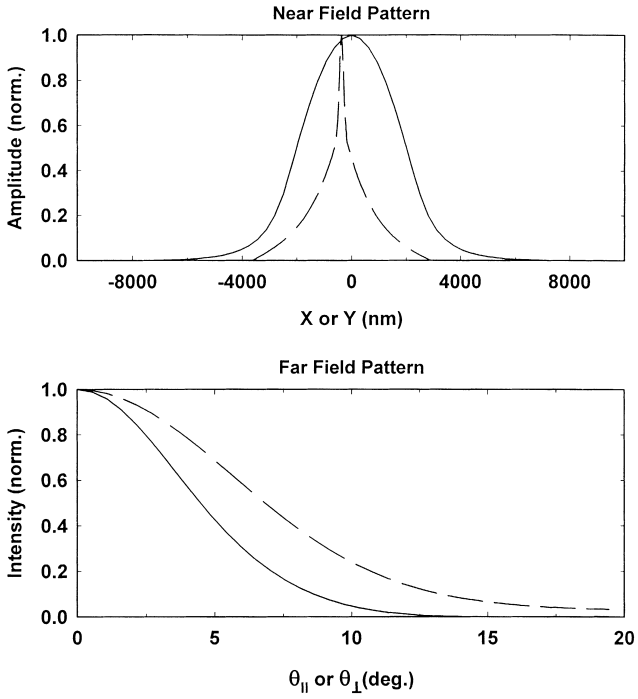

Fig. 9. The same as in Fig. 8. of Laser B.

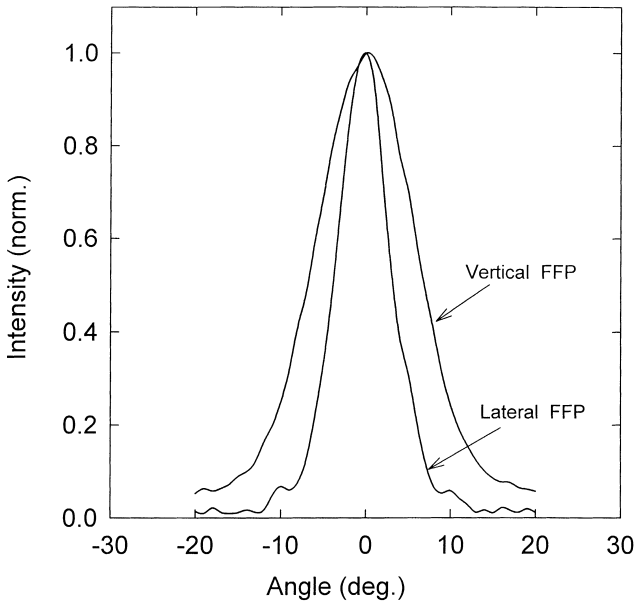

Fig. 10. The measured far-field patterns for the laser sample LM2139. The vertical far-field angle is 13.5° and the lateral far-field angle is 7°.

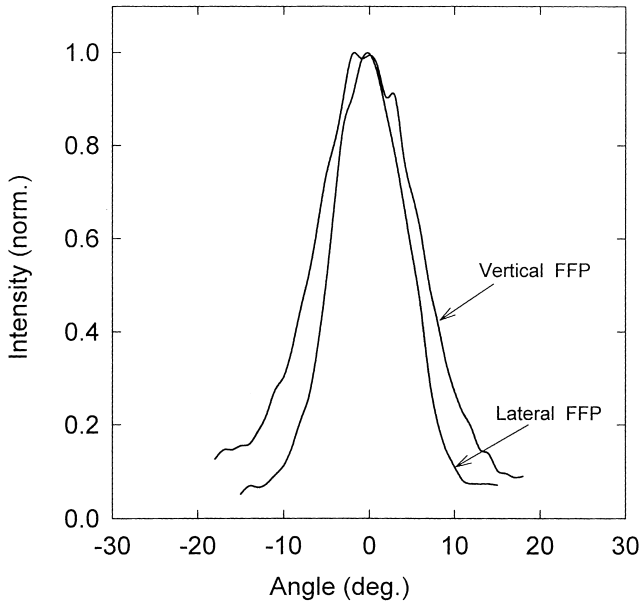

Fig. 11. The measured far-field patterns for the laser sample LM2925. The vertical far-field angle is 14.5° and the lateral far-field angle is 10.5°.

cladding thickness is 3000 Å. For LM2925, the stripe width is estimated to be 5 μm and the external cladding thickness is 1500 Å.

The far-field pattern for LM2139 and LM2925 are shown in Figs. 10 and 11, respectively. For LM2139, the far-field angle is 7° laterally and 13.5° vertically, with an aspect ratio of 1.93. While for LM2925, the far-field angle is 10.5° laterally and 14.5° vertically, with an aspect ratio of 1.38. These experimental results agree very well with the simulation results presented above. So the simulation technique developed here provides us a very powerful tool for designing narrow beam stripe geometry lasers. We should mention that based on our simulation the far-field aspect ratio could be further reduced if the thickness of the cladding layers is further increased. If the cladding thickness is increased from 3 to 6 μm, an aspect ratio of $1.16(\theta_{\perp}/\theta_{\parallel} = 9.8°/8.5°)$ can be achieved.

4. Conclusion

We have analyzed the 2D optical field distribution for lasers with small vertical beam divergence. Discrete spectral index method was used for the 2D simulation. While other simulation methods such as effective index method and finite difference method either fail to give accurate results or are impractical in real calculation, the discrete spectral index method provides an

efficient and accurate way to simulate the mode characteristics of the lasers with small beam divergence. Very good agreement was obtained between the calculated results and the experimental results. Simulation also indicates that for this type of lasers with extended cladding thickness, deeply etched ridge and optimum stripe width, near symmetric beam for optical coupling can be obtained.

Acknowledgement

This work is supported by the National Science Council of the Republic of China under contract NSC89-2218-E009-055.

References

Adams, M.J. *An Introduction to Optical Waveguides* (Chap. 2), John Wieley & Sons, 1981.
Afromowitz, M.A. *Solid State Comm.* **15** 59, 1974.
Barrodale, I. and K.B. Wilson. *J. Comp. Appl. Math.* **4** 159, 1978.
Berry, G.M., S.V. Burk, C.J. Smartt, T.M. Benson and P.C. Kendall. *IEE Proc. J.* **142** 66, 1995.
R.H. Clarke. *Bell Syst. Tech. J.* **62** 2885, 1983.
Lin, G., S.T. Yen, C.P. Lee and D.C. Liu. *IEEE Photon. Technol. Lett.* **8** 1588, 1996.
Robson, P.N., P.C. Kendall. *Rib Waveguide Theory by the Spectral Index Method*, Research Studies Press, 1990.
Temmyo, J. and M. Sugo. *Electron. Lett.* **31** 642, 1995.
Yen, S.T. and Lee, C.P. *IEEE J. Quantum Electron*, **32** 1588, 1996.
Ziari, M., J.-M. Verdiell and D.F. Welch. In: Proceedings of the *IEEE Lasers Electro-Optic Society Annual Meeting*, *LEOS'95*, San Francisco, CA, October 1995, pp. 5–6.